ACS APPLIED MATERIALS & INTERFACES

Research Article

Cite This: ACS Appl. Mater. Interfaces 2019, 11, 40232−40242

www.acsami.org

Wearable, Stretchable, Transparent All-in-One Soft Sensor Formed from Supersonically Sprayed Silver Nanowires

Hong Seok Jo,[†,§] Seongpil An,[‡,§] Chan-Woo Park,[†] Deok-Yoon Woo,[†] Alexander L. Yarin,[*,‡] and Sam S. Yoon[*,†]

[†]School of Mechanical Engineering, Korea University, Seoul 02841, Republic of Korea

[‡]Department of Mechanical and Industrial Engineering, University of Illinois at Chicago, 842 West Taylor Street, Chicago, Illinois 60607-7022, United States

Supporting Information

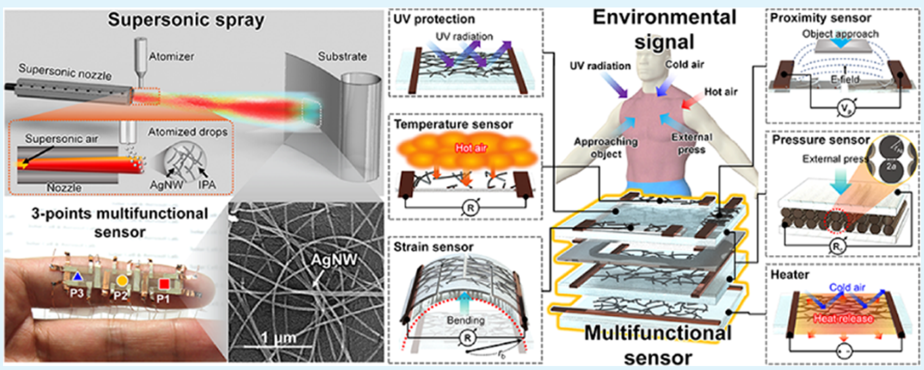

ABSTRACT: The demand for wearable, stretchable soft electronics for human−machine interface applications continues to grow given the potential of these devices in humanoid robotics, prosthetics, and health-monitoring devices. We demonstrate fabrication of multifunctional sensors with simultaneous temperature-, pressure-, proximity-, and strain (or bending)-sensing capabilities, combined with heating and UV-protection features. These multifunctional sensors are flexible, light, and transparent and are thus body-attachable. Silver nanowires are supersonically sprayed on a large-scale transparent and flexible roll-to-roll substrate. The junctions between nanowires are physically fused by a strong impact resulting from supersonic spraying, which promotes adhesion and efficient deposition of the nanowire network. Accordingly, nanowires are strongly interconnected, facilitating efficient propagation of electric signals through the fused nanowire network, which allows simultaneous operation of such sensors while maintaining significant transparency. These multifunctional sensors are mechanically durable and retain long-term stability. A theoretical discussion is provided to explain the respective mechanisms of heating and proximity, pressure, and strain sensing.

KEYWORDS: *wearable, flexible, transparent, multifunctional sensors, UV protection, heater, nanowires, supersonic spraying*

1. INTRODUCTION

The Internet of Things comprises sensors that are interfaced to the internet, which transmit data from sources in real-time.[1] These sensors are installed on electronics or/and human bodies to monitor their status or physical conditions. Although privacy issues remain a concern, in general, transmission or sharing of these large data sets is functional for assisting patients with medical needs or improving the operation of electronic products for consumers.[2,3] In particular, electronic skin (e-skin) has received much attention because it can be used to monitor patients with medical needs and can be used as artificial intelligence skin for humanoid robots.[4,5] The e-skin mimics the human somatosensory system that perceives external stimuli, which are converted into electrochemical signals through neural trails that facilitate sensing of temperature, pressure, strain, humidity, heat, and proximity. Thus, an ideal e-skin must mimic simultaneous execution of these multioperations. In addition, an ideal e-skin must be soft, stretchable, flexible, bendable, and wearable to allow it to fit over surfaces with high curvatures, such as finger joints and elbows, for use in wearable devices,[6,7] prostheses,[8−10] soft robots,[11,12] and health care[13,14] applications. Often, these health-related sensors are installed on display panels or clothes, in which case the transparency of the sensors is desired for practical and esthetic purposes. In short, the e-skin sensors must be multifunctional, flexible, stretchable, transparent, and capable of simultaneous operations.

Previous e-skin sensors are capable of sensing either one or two features. Thus far, pressure,[15−17] temperature,[18−20] strain,[21,22] pressure−strain,[23−25] or pressure−temperature,[26,27]

Received: July 22, 2019
Accepted: October 1, 2019
Published: October 1, 2019

DOI: 10.1021/acsami.9b12847
ACS Appl. Mater. Interfaces 2019, 11, 40232−40242

sensing have been mimicked using various nanomaterials and nanofabrication techniques.[28−30] However, sensors with three or more features are scarce.[28,29] Furthermore, simultaneous detection of multiple stimulus inputs has not been demonstrated.[23,26] In addition, sensors are often nontransparent, hindering their use as supplementary electronics in e-textiles.[27,31] Mechanical durability and stable operation with high sensing accuracy are other challenges to be confronted and overcome. From the practical perspective, the manufacturing costs must be lowered via the development of simple, rapid, and large-scale fabrication processes for commercialization.

Herein, we demonstrate fabrication of transparent, flexible, and stretchable multifunctional sensors comprising supersonically sprayed silver nanowires (AgNWs). Supersonic spraying is a rapid, nonvacuum, binder-free deposition process that can be easily scaled-up for mass production via a roll-to-roll process.[32,33] The fabricated sensor is capable of simultaneously sensing pressure, temperature, strain, and proximity. In addition, this e-skin sensor features a heating mode and thus can warm the surface on which it is installed. Because silver is capable of blocking UV rays, the area under the sensor is free of UV rays and electromagnetic interference, which is certainly an additional benefit of such multifunctional sensors.

2. EXPERIMENTAL METHODS

2.1. Materials. For manufacturing transparent electrodes for heating and temperature- and pressure-sensing functions, silver nanowires (AgNWs with the average diameter and length of 20 nm and 10 μm, respectively) were prepared as a suspension as follows. The AgNW precursor (Aiden, Republic of Korea) dispersed at 0.15 wt % in isopropyl alcohol (IPA) was diluted with IPA (Duksan, Republic of Korea) to a 3:1 weight ratio (IPA/precursor). A poly(dimethylsiloxane) (PDMS) plate was prepared by mixing a silicone elastomer (01064291, Dow Corning) and a curing agent (01015311, Dow Corning) in a 10:1 ratio.

2.2. Sensor Fabrication. Humans are permanently exposed to various environmental stimuli, such as UV light, heat, moisture, external objects, and external forces, as illustrated in Figure 1, and this information can be usually detected by the human nervous system. However, prolonged exposure to these hazardous external environments and high exposure levels can lead to significant damages to the human nervous system. To prevent such damage, the external environments should be recognized in advance through the sensing functions of human skin. The advanced multifunctional sensor developed in this study, which consisted of six sensing functions, is inspired by the subcutaneous receptors of human skin, as illustrated in Figure 1.

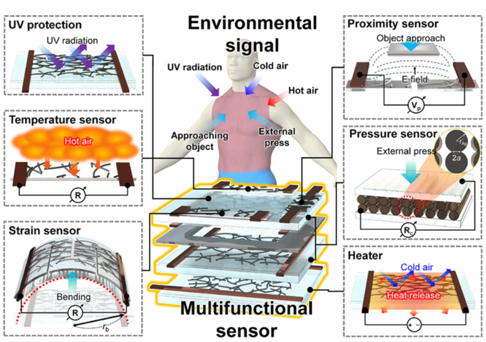

Figure 1. Illustration of a transparent and flexible multifunctional sensor for detecting environmental stimuli, with UV-protection and heating capabilities.

The uppermost layer of the sensor consists of the temperature, strain, and proximity sensors, which can detect the surrounding atmosphere temperature, bending, and an approaching object, respectively. The second and third layers function as a pressure sensor based on changes in the electrical resistance due to a contact between the two layers upon application of an external force. The lowermost layer is a transparent heater that can protect skin against the cold surrounding atmosphere and maintain constant body temperature by Joule heating. Finally, all layers composed of AgNWs can protect skin from exposure to ultraviolet (UV) light.

Figure 2a,b depicts the fabrication process of AgNW transparent conducting films (TCFs), which are not only capable of sensing temperature, proximity, pressure, and strain but also possess heating and UV-protection capabilities. First, a poly(ethylene terephthalate)/poly(dimethylsiloxane) (PET/PDMS) substrate was prepared by pouring PDMS liquid onto a PET film and leaving it until solidified for 1 day at room temperature (the top-left image in Figure 2a). Second, a mask (3 cm × 2.5 cm of the square hole) was positioned on the prepared PET/PDMS substrate and then the surface of the PET/PDMS substrate was coated with AgNWs by supersonic cold spraying under the following conditions (the bottom-left image in Figure 2a): The operating stagnation pressure and the preheating temperature were set to 4 bar and 200 °C, respectively, for forming a supersonic air jet from the de Laval nozzle.[33,34] The flow rate of the AgNW suspension, which was atomized to the supersonic air stream by an atomizer and a syringe pump (Legato 210, KDS), was 1.2 mL min^{-1}, and the scanning speed of the stage for coating the whole area of the PET/PDMS substrate was 4 cm s^{-1} (see Figure 2c,d). Note that the procedure for the formation of the AgNW network by supersonic cold spraying is presented in detail elsewhere.[33,35] After separating the mask from the AgNW-coated substrate, the copper (Cu) electrodes were attached to each side of the AgNW-coated PET/PDMS substrate with a silver paste (ELCOAT A-200, CANS, Japan; see the center image in Figure 2a). Finally, the AgNW TCF was dried in an oven (PMF-3, Lab House, China) for 5 h at 50 °C to solidify the silver paste.

Additional processes for fabricating each layer of temperature, proximity, and strain sensors were required before assembling multiple layers for the complete multifunctional sensor. The layers for temperature, proximity, and strain sensors were made by the AgNW TCF whose dimensions were 2 cm × 0.5 cm. The middle portion of the AgNW TCF was completely cut for its use as a proximity sensor for inducing the fringe capacitor effect in which the capacitance increases when an object is approaching. By contrast, the strain sensor was fabricated by having a single half-cut on one side of the AgNW TCF for increasing an electrical resistance based on the fact that the half-cut zigzagged pattern had a narrower and longer surface (cf. Figure 2a).[36−38] Then, the processed layers were assembled as shown in Figure 2b. First, the layer of AgNW TCF for the heating function was placed at the lowermost part of the multifunctional sensor. Next, the second and third layers of AgNW TCFs were superimposed onto the first layer with a framelike separator (PET, 2 cm × 1.5 cm × 0.02 cm), which was positioned between the second and third layers. Finally, the AgNW TCF, cut AgNW TCF, and slashed AgNW TCF, which, respectively, function as the temperature, proximity, and strain sensors, were placed onto the top part of the multifunctional sensor. This order of the layout prevents any nontransparent parts to be located in the middle of the sensor so that the transparency of the sensor is maintained (cf. Figure S1a).

2.3. Characterization. The morphologies of the AgNWs on PET were identified using a scanning electron microscope (SEM, S-5000, Hitachi, Japan). The transmittance (T) and sheet resistance (R_s) of specimens were explored using an ultraviolet−visible spectrophotometer (Optizen POP, Mecasys, Republic of Korea) and a sheet-resistance meter (FPP-400, Dasol Eng., Republic of Korea), respectively. Variations in electrical properties of the multifunctional sensors, such as resistance (R) and voltage (V), were measured using a source meter (2430 SMU, Keithley) with four probes. Note that, in the case of the proximity layer of the sensor, V was simultaneously

DOI: 10.1021/acsami.9b12847
ACS Appl. Mater. Interfaces 2019, 11, 40232−40242

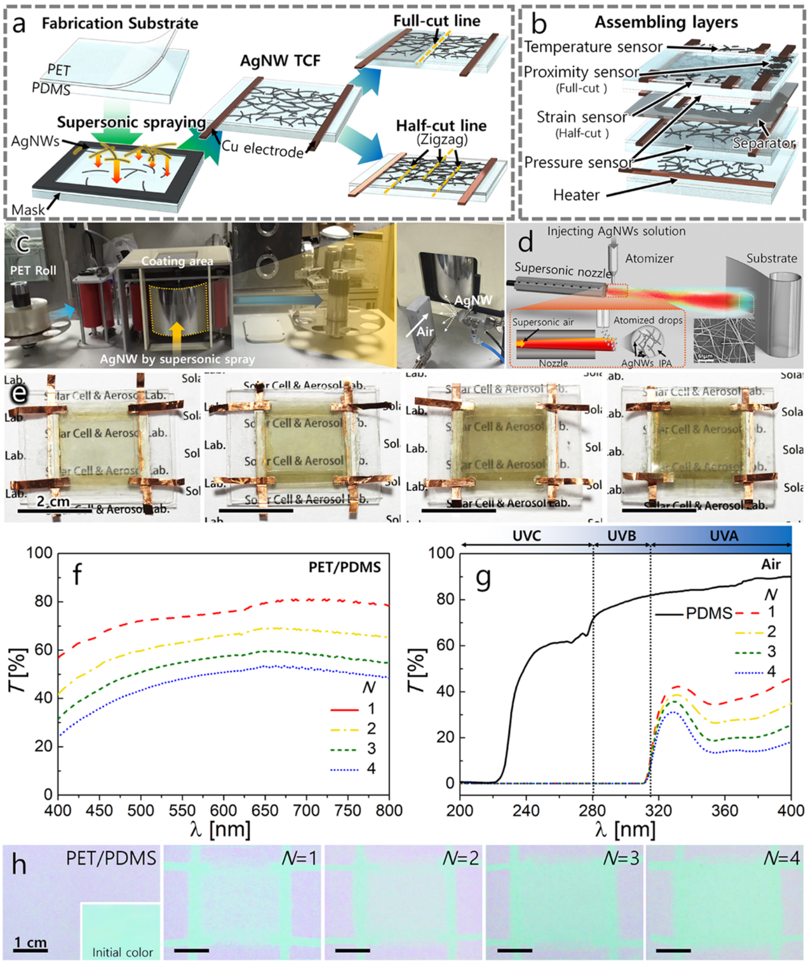

Figure 2. (a) Schematic of the fabrication process for AgNW TCF (center), cut AgNW TCF (top right), and slashed AgNW TCF (bottom right). (b) Illustration for the assembly of a multifunctional sensor. (c) Roll-to-roll process and (d) schematic of the AgNW coating using the supersonic spray. (e) Photos of the multifunctional sensor with increasing N. Transmittance of the multifunctional sensor based on (f) PET/PDMS and (g) air. (h) Color change of UV-detectable paper in response to UV radiation from 315 to 365 nm with increasing N. N is the number of spraying sweeps.

measured by changing the normal mode to the pulse mode in the source meter by supplying a square-pulsed current. The surface temperature (T_h) of the heater layer of the sensor and the surrounding temperature (T_∞) of the sensor (which was monitored to evaluate performance as a temperature sensor) were measured using a data recorder (MV 1000, YOKOGAWA, Japan) with a thermocouple (K-type). The bending and tensile tests of the strain sensor were performed using the testing machine (COAD. 722, Ocean Science, Republic of Korea), where the bending and the stretching rates were 15 and 5 mm min^{-1}, respectively.

3. RESULTS AND DISCUSSION

3.1. Transmittance and UV Protection of a Multifunctional Sensor. Surface morphologies and the corresponding photos of the silver nanowire transparent conducting films (AgNW TCFs) with the varying number of spraying sweeps (N) are shown in Figure S1b. With increasing N, the network of deposited AgNWs on a substrate became denser by filling the space around the crossed nanowires, where the ratio of the area of the deposited AgNWs to the total surface area of the specimen increased from 37 to 42, 48, and 55% as the value of N varied from 1 to 2, 3, and 4, respectively (cf. Figure S1c).[39,40] As a result, the transmittance (T) of the single AgNW TCFs at the wavelength of light (λ) of λ = 550 nm decreased from T = 96 to 70% with an increase of the density of the deposited AgNWs; see Figure S1d.[40] On the other hand, both values of the sheet resistance (R_s) and resistance (R_0) decreased with increasing N (Table 1). Although the value of

Table 1. Electrical Properties of the AgNW TCFs

	N	R_0 (Ω)	R_s (Ω sq^{-1})	T (%)
AgNW TCFs	1	68.4	82.5	95.7
	2	40.1	62.2	84.5
	3	23.4	38.5	77.4
	4	14	11	70

T of a single AgNW TCF decreased to 70%, it should be emphasized that the resulting assembled multifunctional sensors were sufficiently transparent to read underneath of the letters in all N cases (Figure 2e). Given that the value of T of a bare PET/PDMS substrate was T = 100%, those of the assembled sensors varied from T = 74 to 63, 55, and 48% with increasing N, as shown in Figure 2f.

Figure 2g,h demonstrates the feasibility of UV protection of our multifunctional sensors. Figure 2g shows the T spectra of the assembled multifunctional sensors in the UV spectral range of λ = 200−400 nm.[41] For the bare PDMS substrate, all UV rays penetrated the PDMS substrate, where the value of T

DOI: 10.1021/acsami.9b12847
ACS Appl. Mater. Interfaces 2019, 11, 40232−40242

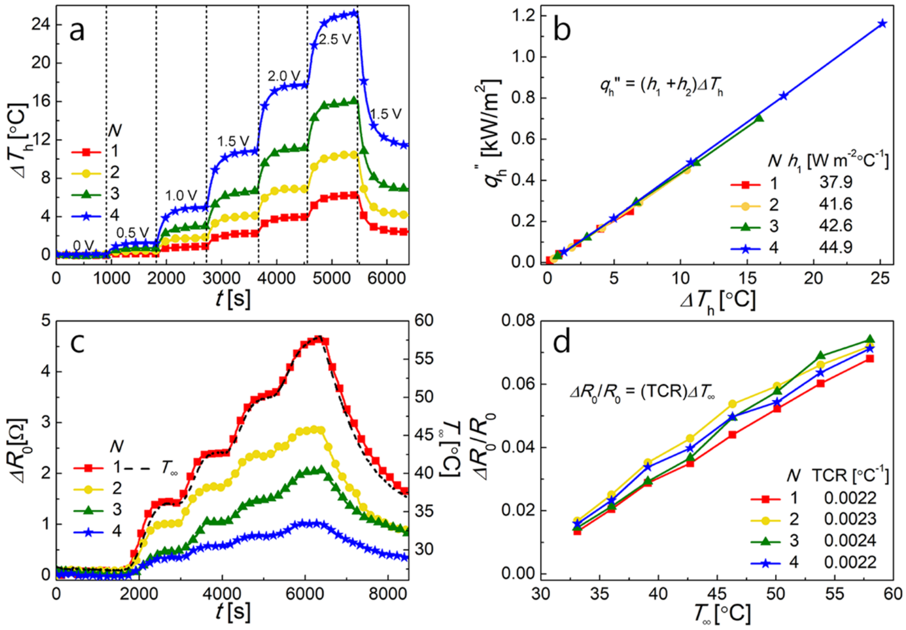

Figure 3. Performances of the multifunctional sensor as a transparent heater and a thermal sensor: (a) heater temperature (T_h) with increasing applied voltage (V_a) and (b) comparison of the heating performance at different values of N. (c) Resistance variation of the temperature sensor with increasing surrounding temperature (T_∞ = the temperature of the thermostat) and (d) sensitivity of the temperature sensor.

ranged from T = 0 to 90%. In contrast to the PDMS case, the UVC light, having a short range of λ and most dangerous rays, and the UVB light, having a medium range of λ and related to tanning, burning, and skin cancer, were completely blocked by the AgNW TCFs.[42−44] However, the slight amount of UVA light, which has a long range of λ, was transmitted through the multilayers of the sensor, with the value of T from T = 0 to 45%.

The first image in Figure 2h shows the response of a UV-sensitive paper against the UV rays. The color of the UV-sensitive paper was initially cyan, whereas the color changed to light-blue upon UV irradiation, as demonstrated using a bare PET/PDMS substrate. As expected, contrary to the bare PET/PDMS substrate, the initial cyan color was maintained when the UV-sensitive papers were covered by the AgNW TCFs, where the UV ray was completely blocked in the case of N = 4.

3.2. Heating and Thermal Sensing.

Figure 3a shows the heating performances of multifunctional sensors fabricated with varying N. The heating was driven by Joule heating when a certain voltage was applied to the AgNW TCF (E3642A 50 W power supply, Agilent).[45] The assembled multifunctional sensor consisting of the AgNWs with the highest value of N revealed the highest heating temperature (T_h), where the temperature was measured by a K-type thermocouple placed on top of the sensor (Figure S2a). The applied voltage incrementally increased with the time interval of Δt = 15 min in the range of $0.5 \le V_a \le 2.5$ V, which resulted in an increase in temperature variation (ΔT_h) up to $\Delta T_h \sim 25$ °C (where $\Delta T_h = T_h - T_\infty$ and the surrounding temperature T_∞ was T_∞ = 26.8 °C). In other words, the heater temperature of the multifunctional sensor reached $T_h \sim 52$ °C. Note that the T_h increased with the increasing applied voltage because the heating power (P_h) is proportional to the voltage squared as $P_h = V_a^2/R_0$, indicating that the sensor based on a high number of N (thus having a small R_0) can supply a high electric power for heating.

The energy balance across a heater layer of the multifunctional sensor, having a conductive−convective cooling without radiation, can be expressed as

$$mc\frac{dT_h}{dt} = -[h_1 + h_2]A(T_h - T_\infty) + P_h \tag{1}$$

where c, m, and A are the specific heat, mass, and surface area of the heater layer, respectively. The h_1 and h_2 are heat transfer coefficients at the outer and inner sides of the heater layer, respectively. The bottommost layer (the inner side) of the sensor was insulated by glass wool. Four layers of the pressure, strain, proximity, and temperature sensors were stacked under the heater layer. Then, T_h is found in eq 1 as[45]

$$T_h - T_\infty = (T_i - T_\infty)\, e^{-t/\tau} + \frac{P_h}{(h_1 + h_2)A}[1 - e^{-t/\tau}] \tag{2}$$

$$\tau = \frac{mc}{(h_1 + h_2)A} \tag{3}$$

where T_i is the initial heater temperature. In the steady state (when time $t \gg \tau$), eq 2 can be reduced as

$$T_h - T_\infty = \frac{P_h}{(h_1 + h_2)A} \tag{4}$$

which yields

$$q_h'' = (T_h - T_\infty)(h_1 + h_2) \tag{5}$$

where the heat flux $q_h'' = P_h/A$. Thus, the conductive−convective heat transfer coefficient at the outer surface can be expressed as

$$h_1 = \frac{q_h''}{(T_h - T_\infty)} - h_2 \tag{6}$$

Here, the value of h_2 at the inner surface is known; see eq S1. It is h_2 = 1.5 W m^{-2} °C^{-1} for all cases. The linear dependence of

DOI: 10.1021/acsami.9b12847
ACS Appl. Mater. Interfaces 2019, 11, 40232−40242

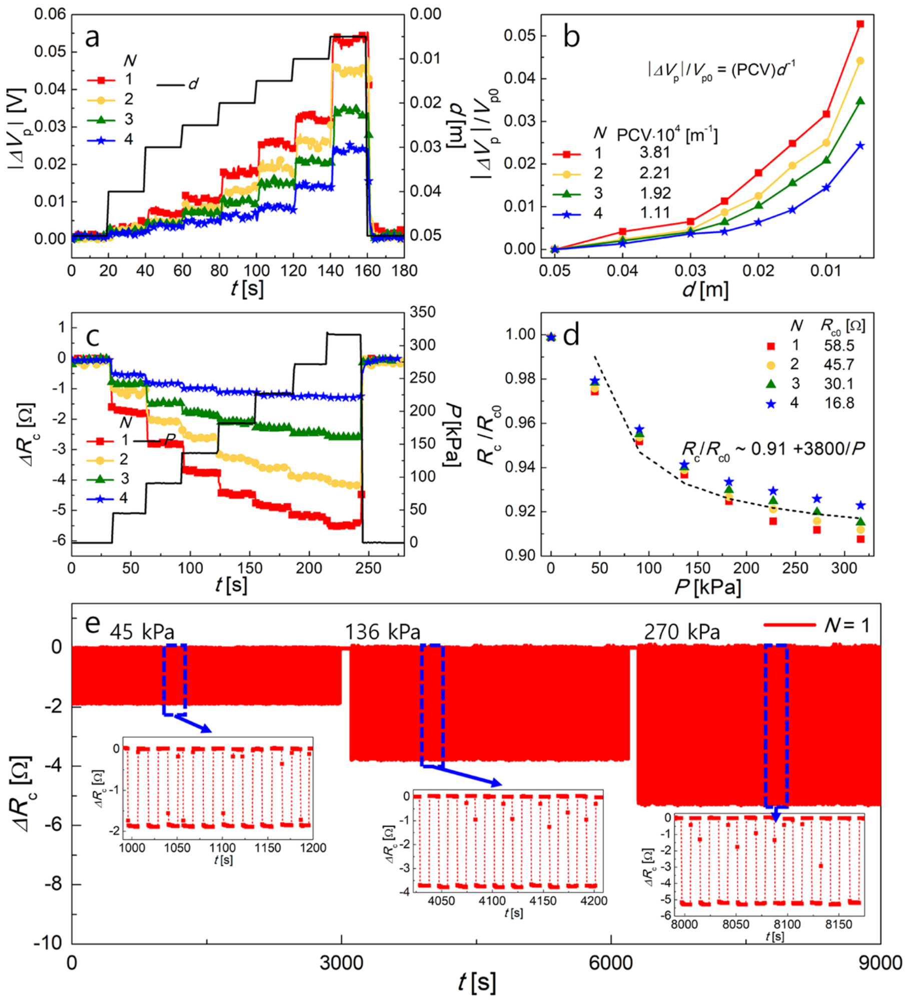

Figure 4. Performances of the multifunctional sensor as proximity and pressure sensors. (a) Voltage response of the proximity sensor with decreasing distance d between the sensor and the object (steel plate) and (b) sensitivity of the proximity sensor with different N. (c) Resistance variation of the pressure sensor with an increase in the value of P from 0 to 316 kPa. (d) Sensitivity of the pressure sensor with different N and (e) stability of the pressure sensor with N = 1 under repetitive pressing/releasing cycles of P = 50, 136, and 270 kPa.

q_h'' on $\Delta T_h = (T_h - T_\infty)$ according to eq 5 is plotted in Figure 3b. The slope of this fit to the data was found and used to evaluate h_1 according to eq 6; cf. Figure 3b. The slope increased slightly with increasing N, but the difference was minor.

Figure 3c shows the resistance changes of the thermal sensor in response to the change in the surrounding (or chamber) temperature T_∞ in the 28−58 °C range, which was measured using the property of the metal that linearly varies with temperature change. Figure S2b shows the positioning of the temperature sensor layer of the multifunctional sensor outward toward the surrounding atmosphere. Note that the heater was thus in contact with the insulator and faced inward; the sensor was placed upside down (cf. Figure S2a,b). While approaching T_∞ = 58 °C, the sensor resistance reached ΔR ~ 4.5 Ω for N = 1. The sensitivity in all cases was estimated by plotting the slope of the ratio $\Delta R/R_0$ versus T_∞, which is known as the temperature coefficient of resistance (TCR). Figure 3d shows that the slope was nearly constant for all cases. Given that the ratio $\Delta R/R_0$ is a normalized value, R_0 diminished with increasing N, which, in turn, maintained a nearly constant value of $\Delta R/R_0$ for all cases. Thus, TCR remained unchanged irrespective of N.

3.3. Proximity Sensor. A proximity sensor is designed to perceive an approaching object by the mechanisms of induction and ultrasonic, optical, and capacitance changes.[46−49] Capacitive proximity sensors are the most suitable for detecting both conductive and nonconductive objects.[47] In the present study, the capacitive sensor was developed, which operated based on two aligned, but disconnected, electrodes, as illustrated in Figure S2c. One electrode detected electrical signals, whereas the other electrode was grounded. This setup induced parasitic capacitance (C_p) between the AgNW electrodes and formed an electric field, as depicted in Figure 1. When an object starts to approach the multifunctional proximity sensor, the formed electric field is disrupted and the voltage between the metal electrodes changes.

The capacitance induced during this electric disruption is denoted here as C_a. That is, the total capacitance is equal to $C_t = C_p + C_a$. The change in the root-mean-square (rms) voltage, ΔV_p, is an indicator of the capacitance change at the approach of the object: $\Delta V_p = V_p - V_{p0}$, where V_{p0} is the initial voltage between the two metal electrodes and the voltage was measured with a voltmeter (2430 SMU, Keithley). Figure S2c depicts an object (a steel plate of 10 cm × 10 cm in size) approaching the multifunctional proximity sensor as the object

DOI: 10.1021/acsami.9b12847
ACS Appl. Mater. Interfaces 2019, 11, 40232−40242

perturbs the electric field formed between the two metal electrodes. A square-pulsed current of I_{rms} = 10 μA with a frequency of 2 kHz was supplied by the source meter and the change in the voltage was measured. The steel plate was initially placed at a distance of d = 0.05 m from the sensor but gradually approached the sensor by Δd = 0.010 and 0.005 m at the intervals of Δt = 20 s; see the solid black line in Figure 4a. At t = 160 s, the object was returned to the initial distance of d = 0.05 m. While changing d, the voltage increased in a stairwell pattern for all cases (Figure 4a). The sensor with N = 1 was the most sensitive to the approaching object, with the greatest change in ΔV_p. The voltage change decreased to zero when the object was returned to the initial position of d = 0.05 m at t = 140 s. Figure 4b compares the sensitivity of the sensors with different values of N. The proximity coefficient of the voltage (PCV) was defined to model the relation between $\Delta V_p/V_p$ and the distance, d, in the following form

$$\frac{|\Delta V_p|}{V_{p0}} = \frac{\mathrm{PCV}}{d} \tag{7}$$

The PCV values are summarized in the inset of Figure 4b. Herein, the sensors with smaller N revealed higher sensitivities (which correspond to larger PCV). The value of V_{p0} remained constant for all cases because the parasitic capacitance is independent of N. Thus, the increase of $|\Delta V_p|/V_p$ with respect to d was notable, as manifested by the values of PCV.

The capacitance and voltage are inversely proportional. The additional capacitance is defined as

$$C_a = \frac{\varepsilon_a A_h}{d} \tag{8}$$

where ε_a and A_h are the dielectric permittivity of air and the area of the horizontal plane of the electrode, respectively. On the other hand, the parasitic capacitance is defined as

$$C_p = \frac{\varepsilon_a A_v}{d_p} \tag{9}$$

where A_v is the area of the vertical plane of the electrode and d_p is the distance between the two electrodes.[50] The root-mean-square (rms) voltage can also be defined as

$$V_p = I_{rms} X_c = I_{rms}\left(\frac{1}{2\pi f}\frac{1}{C_t}\right) \tag{10}$$

$$\Delta V_p = V_p - V_{p0} = \frac{I_{rms}}{2\pi f}\left(\frac{1}{C_p + C_a} - \frac{1}{C_p}\right) = -\frac{I_{rms}}{2\pi f \varepsilon_a}\frac{A_h {d_p}^2}{A_v(A_v d + A_h d_p)} \tag{11}$$

where f is the frequency of the alternating current. In eq 11, all parameters are constant, except for the distance to the approaching object, d. Equation 11 shows that the $|\Delta V_p|$ increases as the d decreases, which was experimentally confirmed as revealed in all N cases in Figure 4a,b. The sensitivity of the multifunctional proximity sensor was the lowest in the case of the largest N. As the value of N increased, the vertical area of the electrode, A_v, also increased because the AgNW layer was thicker at the larger N cases. Accordingly, the value of $|\Delta V_p|$ decreased as described in eq 11. Thus, one can conclude that the sensitivity of the proximity sensor is the highest when the value of N is the lowest.

3.4. Pressure Sensing. The multifunctional pressure sensor was designed by overlaying two AgNW TCFs in contact with each other, as depicted in the inset of Figure 1, where the circular cylinders represent two individual AgNWs with the same radius of r_{Ag}. These two AgNWs make a contact with each other, having a contact length of $2a$ upon applying pressure to the sensor. The contact resistance (R_c) of the multifunctional pressure sensor in this scenario is given by the following dependence[51−53]

$$R_c = \frac{\rho}{2a}\left[1 - 1.42\left(\frac{a}{r_{Ag}}\right) + 0.063\left(\frac{a}{r_{Ag}}\right)^2 + 0.153\left(\frac{a}{r_{Ag}}\right)^3 + 0.2\left(\frac{a}{r_{Ag}}\right)^4\right] \tag{12}$$

where ρ is the AgNW resistivity and a is the half-width of the contact length (or zone) marked in Figure 1. If $r_{Ag} > a$ (which is most likely the case), eq 12 can be reduced to the following form by truncating the higher-order terms

$$R_c \sim \frac{\rho}{2a}\left[1 - 1.42\left(\frac{a}{r_{Ag}}\right)\right] \tag{13}$$

As the applied pressure increases, the contact length ($2a$) between the two adjacent AgNWs also increases, which corresponds to the fact that R_c in eq 13 decreases because of an increase in a. Note that, similarly to the setup used for the temperature sensor (Figure S2b), the AgNW layers detecting the applied pressure face outward (Figure S2d).

The relation between the width of the contact length ($2a$) and the compressive force (F) is given by the solution of Hertz's problem for two cylinders[54]

$$2a = \frac{4}{\sqrt{\pi}}\sqrt{\frac{(1-\nu^2)}{E} r_{Ag} F} \tag{14}$$

where E is Young's modulus and ν is Poisson's ratio of AgNWs.

By substituting this relation in eq 13, the relation between the resistance R_c and the applied pressure ($P = F/2a$) takes the form

$$a = \frac{8}{\pi}\frac{(1-\nu^2)}{E} r_{Ag} P \tag{15}$$

$$R_c = \frac{\rho}{2a}\left[1 - 1.42\frac{8}{\pi}\frac{(1-\nu^2)}{E} P\right] \tag{16}$$

Because E is always much larger than P, the above equations yield $R_c \sim 1/P$. Substituting eq 15 into eq 16 and accounting for the fact that $P/E \ll 1$ one obtains

$$R_c = \frac{\rho}{2a} = \frac{A}{P},\ A = \frac{\rho \pi E}{16(1-\nu^2) r_{Ag}} \tag{17}$$

Taking the logarithmic derivative of eq 17 yields

$$\frac{1}{R_c}\frac{\mathrm{d}R_c}{\mathrm{d}P} = -\frac{1}{P} \tag{18}$$

DOI: 10.1021/acsami.9b12847
ACS Appl. Mater. Interfaces 2019, 11, 40232−40242

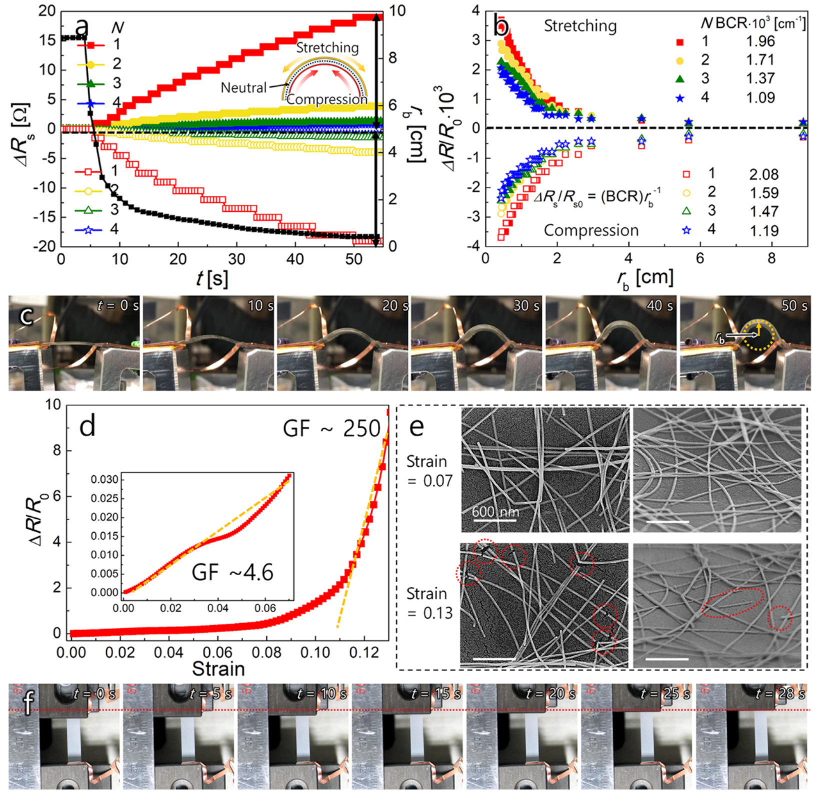

Figure 5. Performances of the multifunctional sensor as a strain sensor. (a) Resistance variation of the strain sensor with increasing N in response to a decrease in the bending radius (r_b), (b) sensitivity of the strain sensor for different cases of N, and (c) photographs of the strain sensor with the decrease of r_b. (d) Resistance variation of the strain sensor with $N = 1$ when it is stretched from 0 to 13%, (e) corresponding SEM images of the strain sensor at the strains of 0.07 and 0.13, and (f) snapshots of the strain sensor for 28 s. It should be emphasized that the ranges of the normalized resistance changes ($\Delta R/R_0$) of the thermal and strain sensors practically do not overlap and thus are distinguishable; cf. (d) here with Figure 3d.

Note also that eq 17 means that the product R_cP is a constant, which is independent of N.

As shown in Figure 4c, we varied the applied pressure from P = 45 to 316 kPa using various weights with an interval of Δt = 30 s for 240 s, after which all weights were removed and no pressure was applied. Note that the initial contact resistances were R_{c0} = 58.5, 45.7, 30.1, and 16.8 Ω for cases of N = 1, 2, 3, and 4, respectively. The reason for this variation was that the contact surface area between the deposited AgNWs increased as greater numbers of AgNWs were deposited with increasing N, thus causing a decrease of R_c. Figure 4c shows that ΔR_c decreased with the increasing P for all cases. When the value of P increased, the value of R_c decreased, thereby ΔR_c ($=R_c - R_{c0}$, where R_{c0} was fixed) also decreased. This pattern was consistent for all N cases. The above theoretical model also confirms this pattern.

As demonstrated in eq 17, the contact resistance R_c is proportional to $1/P$. Figure 4d shows the plot of the dimensionless contact resistance R_c/R_{c0} versus P, which demonstrates that indeed $R_c \propto 1/P$. For $P \leq 150$ kPa, there is no distinction between the cases with different N, as the theory predicted in eq 17. However, some slight dependence on N appears at $P \geq 150$ kPa. At higher pressures, contacts between AgNWs are interlinked in a random network, which significantly deviates from the theoretical assumption of the contact of two perfectly aligned cylinders. As N increases, the contact area between cylinders becomes greater than predicted and thus the value of R_c would decrease. However, the value of R_c decreased as N increased in Figure 4d. This probably indicates that the alignment pattern also changed as N increased. The sensitivity in the case of N = 1 was the highest among all of the cases.

Figure 4e indicates the stability of the pressure sensor in terms of ΔR_c as a function of cycles, where the cyclic pressure was increased to 50, 136, and 270 kPa every 150 cycles and the total of 450 cycles were performed for Δt = 9000 s. There was no discernible sign of degradation for the pressure sensing (Figure 4e).

3.5. Strain (Bending) Sensing. Considering the potential applications of the multifunctional sensor, it should be soft enough to be easily attachable onto various substrates having a high curvature and high roughness, for example, elbows, finger joints, and knees of humans. The strain sensor is expected to respond to a bending amplitude in such locations, which can be detected by exploring a resistance variation of the sensor. The resistance change of metals is related to the geometrical deformation of the metal structure by applied mechanical stresses.[55−57] Considering a metal tape with a length of l, a cross-sectional area of A, and a specific resistivity of ρ, the resistance across this metal tape is defined as

$$R = \frac{\rho l}{A} \tag{19}$$

The differential of eq 19 yields for a deformed sensor

$$\frac{\mathrm{d}R}{R} = -\frac{\mathrm{d}A}{A} + \frac{\mathrm{d}l}{l} + \frac{\mathrm{d}\rho}{\rho} \tag{20}$$

DOI: 10.1021/acsami.9b12847
ACS Appl. Mater. Interfaces 2019, 11, 40232−40242

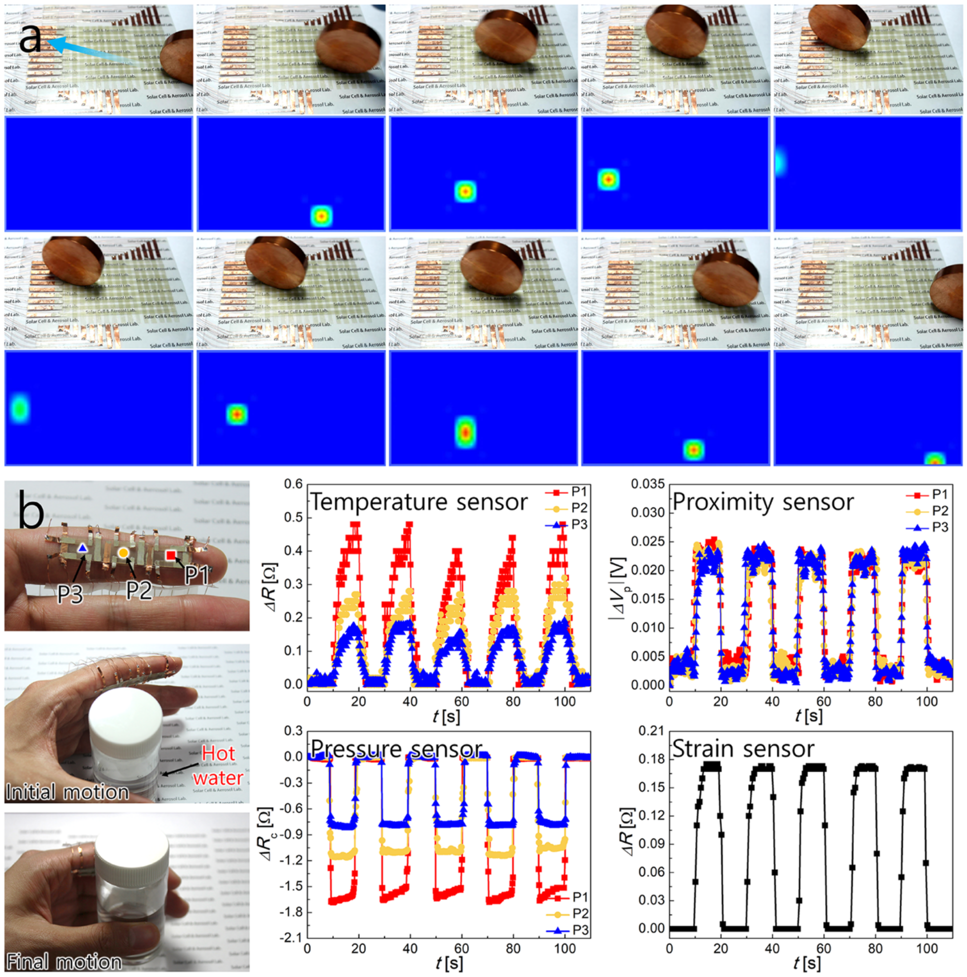

Figure 6. (a) Snapshots of the rolling Cu disc on the active-matrix pressure sensor and the corresponding visualization images. (b) Photographs of the three-point multifunctional sensor and the corresponding results of the pressure, temperature, proximity, and strain sensing. The sensor is deposited on bare human skin.

Using Poisson's ratio, ν, in the following expression

$$\frac{dA}{A} = -2\nu\frac{dl}{l} \tag{21}$$

Equation 20 can be expressed as

$$\frac{dR}{R} = (2\nu + 1)\varepsilon + \frac{d\rho}{\rho} = \left[(1 + 2\nu) + \frac{1}{\varepsilon}\frac{d\rho}{\rho}\right]\varepsilon = \eta_s\varepsilon \tag{22}$$

where $\varepsilon = dl/l$ is the strain and η_s is the sensitivity factor [or the gauge factor (GF)].[58−60] Note that according to ref 61, $\varepsilon = h/(2r_b)$, where h is the strain sensor thickness and r_b is the radius of curvature on the bent surface. The latter yields the dependence of the resistance of the radius of curvature in the following form

$$\frac{dR}{R} = \eta_s\frac{h}{2r_b} \tag{23}$$

The normalized change in the resistance (dR/R) in eq 23 is positive during stretching and negative during compression. When the AgNWs face upward and the substrate is bent up or down in a concave form, the process is, respectively, referred to as stretching or compression. Similarly, if the AgNWs face downward and the substrate is bent up or down in a concave form, the process is, respectively, referred to as compression or stretching. Accordingly, the radius of curvature should be positive and negative. In this case, $r_b = \infty$ and thus $dR = 0$. As in bar bending, there always is a neutral line in the middle, which does not change its length when the sensor bends. On the other hand, the sensor elements that are located outwardly of the neutral line are stretched and those located inwardly are compressed. These stretching and compression motions are depicted in Figure 5a, wherein the AgNW TCF underwent bending while the bending radius (r_b) was reduced. When the r_b was reduced from r_b = 8.9 to 0.43 cm, the change in the resistance variation (ΔR) increased during stretching and decreased during compression.

The snapshots in Figure 5c show the bending process of the multifunctional sensor over 50 s, in conjunction with Figure 5a,b. Similarly to the temperature, proximity, and pressure sensors, the case with N = 1 revealed the most sensitive response to bending both at stretching and compression. Figure 5b shows the data for the normalized resistance ($\Delta R/R_0$) with respect to r_b. According to eq 23, $\Delta R/R_0$ is inversely proportional to r_b with the bending coefficient of resistance (BCR) being equal to $\eta_s h/2$. The corresponding BCR values are listed in Figure 5b for all values of N. Using the values of BCR, the sensitivity values are estimated as η_s = 0.020, 0.017, 0.014, and 0.011 for N = 1, 2, 3, and 4, respectively, for the

DOI: 10.1021/acsami.9b12847
ACS Appl. Mater. Interfaces 2019, 11, 40232−40242

stretching case. Similarly, for the compression case, the corresponding sensitivity values were η_s = 0.021, 0.016, 0.015, and 0.012.

Figure S3a demonstrates the bending performance of the strain sensor for 1000 cycles that correspond to the time period of Δt = 10 000 s. The sensors were attached to the skin of a human finger by spreading Ecoflex (Ecoflex 00-10, Smooth-On) onto the underside of the sensor, which is softer and more adhesive than PDMS;[62,63] one sensor was attached to the upper side of a finger, whereas the other sensor was attached to the lower side, as described in Figure S3a. The corresponding cyclic responses exhibited in Figure S3a showed no discernible degradation in the electrical resistance, demonstrating the superiority in performance. Furthermore, as revealed in Figure S3b,c, the deposited AgNWs in the sensor were not peeled off even after 1000 cycles.

As interest in the wearable devices has grown exponentially in different industries, such as those manufacturing sports devices, electronic skins (e-skins), and health-monitoring systems, the demand for product stretchability has also risen. Accordingly, the gauge factor (GF), which describes the relation between the electrical resistance and the mechanical strain, is an essential property to demonstrate sensor sensitivity and superiority. The gauge factor can be expressed as GF = $dR/\varepsilon R$ via eq 22.

Figure 5d,e shows the normalized resistance ($\Delta R/R_0$) and SEM images of the strain sensor with N = 1 as the strain varied from 0 to 13%. Also, the corresponding snapshots of the strain sensor with the dimensions of 1.8 cm × 0.5 cm × 0.1 cm attached to the silicone film under stretching are shown in Figure 5f. The distinguishable changes in $\Delta R/R_0$ were observed during stretching: the value of $\Delta R/R_0$ in the strain range of 0−0.07 gradually increased from 0 to 0.3, whereas that in the strain range of >0.08 steeply increased and finally reached the value of 10 at the strain of 0.13. In the strain range of 0−0.07, the GF was 4 and the deposited AgNWs were well attached on the film without any damage (Figure 5e), whereas in the strain range of 0.11−0.13, the GF was as high as 250 and a number of damaged AgNWs were observed (Figure 5e, highlighted by red ovals).

Figure S3d illustrates the repeatability of the strain sensor during 1000 cycles of stretching at the fixed strain of 0.05. Although the resistance of the strain sensor slightly increased with cycling, the cyclic response was very stable because the variations in the resistance at the initial 10 and final 10 cycles were the same: 20 Ω. Moreover, the deposited AgNWs were rarely damaged and adhered well to the substrate during 1000 cycles, as revealed in the inset SEM images in Figure S3d.

3.6. Simultaneous Multifunctional Operation. It is imperative that all the features of the sensor operate simultaneously. We demonstrated the simultaneous operation of multifunctional features of the developed sensor, where no special demonstration of the UV protection is required as this feature is inherent for the AgNW TCFs. Here, the simultaneous multifunctional operation of the thermal, proximity, strain, and pressure sensing is demonstrated.

Figure 6a shows the rolling Cu disc on an active-matrix pressure sensor (N = 4 and the size of 9 cm × 5 cm with 10 × 16 grids, see Figure S3a). This active matrix can detect the applied pressure through the electronic circuit, which is also able to convert external physical stimuli into digital signals. The Cu disc was rolled back and forth in the diagonal direction. The pressured locations were marked by the circuits and the contour images were juxtaposed with the corresponding photos in Figure 6a; also see Movie S1.

Figure 6b shows the multifunctional sensor attached onto a finger joint by spreading Ecoflex onto the underside of the sensor. The sensor size was 4 cm × 0.5 cm, and three sensors were aligned at three different zones: P1, P2, and P3. Each sensor was fabricated with N = 4 and consisted of four layers, which were designed to sense variations of temperature, proximity, pressure, and strain (or bending). In Figure 6b, a glass vial filled with hot water (60 °C) was grabbed by a hand with the multifunctional sensor on a single finger. When the container had been grabbed, the corresponding data from the sensors for all three zones (P1, P2, and P3) were plotted. A total of five cycles were repeated and the results were highly repeatable, except the variations caused by the human motion. The pressure was the highest at location P1 near the fingertip where contact with the surface of the vial was the tightest and thus the temperature sensitivity was accordingly the highest at this point. In the case of the proximity sensor, the same distance to all three locations was similar as the sensors approached the vial and thus nearly no difference in the voltage data (ΔV_p) was observed.

4. CONCLUSIONS

Silver nanowires (AgNWs) were supersonically sprayed onto transparent flexible substrates for the fabrication of multifunctional sensors that can monitor various variations of external stimuli, including temperature, pressure, strain, and proximity. Moreover, this sensor is also capable of heating and UV protection. The resistance of the sensor changed in response to external stimuli such as temperature, pressure, and strain (or bending), whereas the capacitance (or voltage) of the sensor changed upon the variation of the proximity to an object. UV radiation in the 200−320 nm wavelength range was completely blocked. In the heater mode, the temperature of the sensor could be increased in the 5−25 °C range upon applying a voltage of 2.5 V or less. The change in the sensor resistance was approximately 5 Ω or less when the sensor was subjected to the atmospheric temperature variations of 30 °C or less. The temperature coefficient of resistance was nearly constant for all sensors. The voltage increased within the 0−0.06 V range for proximity sensing of an approaching object. The sensor with the highest transparency was the most sensitive in responding to the approaching object. The pressure sensor functions by a change in the resistance in the 0−6 Ω range due to the application of a pressure of ∼350 kPa or less. Here, again, the sensor with the highest transparency was the most sensitive to the external pressure stimulus. The strain or bending operation was monitored based on changes in the resistance in the range of 20 Ω or less. This multifunctional sensor is body-attachable for use in artificial intelligence robotics and electronic skins and possesses great flexibility and transparency.

■ ASSOCIATED CONTENT

Supporting Information

The Supporting Information is available free of charge on the ACS Publications website at DOI: 10.1021/acsami.9b12847.

Side-views of the multifunctional sensor, SEM images, photos, the ratio of the area of the deposited AgNWs, and transmittance (T) spectra of the AgNW TCFs with N = 1, 2, 3, and 4 (Figure S1); illustration of the measurement methods (Figure S2); cyclic test of the

DOI: 10.1021/acsami.9b12847
ACS Appl. Mater. Interfaces 2019, 11, 40232−40242

upper and lower strain sensors with $N = 1$ in response to finger bending and the SEM images of the AgNWs on the substrate at the beginning and after 1000th cycles of bending; resistance variation of the strain sensor with $N = 1$ at the strain = 0.07 for 1000 cycles and the corresponding SEM images at the beginning and after the final 1000th cycle; photo of the active-matrix pressure sensor and the corresponding electric circuit board; photo of the three-point multifunctional sensor and the corresponding illustration of the structure and functional diagram (Figure S3) (PDF)

Visualized response of the active-matrix pressure sensor (Movie 1) (MP4)

AUTHOR INFORMATION

Corresponding Authors

*E-mail: ayarin@uic.edu (A.L.Y.).

*E-mail: skyoon@korea.ac.kr (S.S.Y.).

ORCID

Alexander L. Yarin: 0000-0001-8032-2525

Sam S. Yoon: 0000-0002-9031-4198

Author Contributions

[§]H.S.J. and S.A. contributed equally to this work.

Notes

The authors declare no competing financial interest.

ACKNOWLEDGMENTS

This research was supported by the Technology Development Program to Solve Climate Changes of the National Research Foundation (NRF) funded by the Ministry of Science, ICT & Future Planning (NRF-2016M1A2A2936760, NRF-2017R1A2B4005639, and NRF-2013R1A5A1073861).

REFERENCES

(1) Ezechina, M.; Okwara, K.; Ugboaja, C. The Internet of Things (Iot): A Scalable Approach to Connecting Everything. *Int. J. Eng. Sci.* **2015**, *4*, 09−12.

(2) Gubbi, J.; Buyya, R.; Marusic, S.; Palaniswami, M. Internet of Things (Iot): A Vision, Architectural Elements, and Future Directions. *Future Gener. Comput. Syst.* **2013**, *29*, 1645−1660.

(3) Tan, L.; Wang, N. In *Future Internet: The Internet of Things*, 2010 3rd International Conference on Advanced Computer Theory and Engineering (ICACTE); IEEE: Chengdu, China, 2010; Vol. 5, pp V5-376−V5-380.

(4) Chortos, A.; Liu, J.; Bao, Z. Pursuing Prosthetic Electronic Skin. *Nat. Mater.* **2016**, *15*, 937−950.

(5) Chortos, A.; Bao, Z. Skin-Inspired Electronic Devices. *Mater. Today* **2014**, *17*, 321−331.

(6) Lee, H.; Hong, Y. J.; Baik, S.; Hyeon, T.; Kim, D. H. Enzyme-Based Glucose Sensor: From Invasive to Wearable Device. *Adv. Healthcare Mater.* **2018**, *7*, No. 1701150.

(7) Trung, T. Q.; Ramasundaram, S.; Hwang, B. U.; Lee, N. E. An All-Elastomeric Transparent and Stretchable Temperature Sensor for Body-Attachable Wearable Electronics. *Adv. Mater.* **2016**, *28*, 502−509.

(8) Roland, T.; Wimberger, K.; Amsuess, S.; Russold, M. F.; Baumgartner, W. An Insulated Flexible Sensor for Stable Electromyography Detection: Application to Prosthesis Control. *Sensors* **2019**, *19*, No. 961.

(9) Gerratt, A. P.; Michaud, H. O.; Lacour, S. P. Elastomeric Electronic Skin for Prosthetic Tactile Sensation. *Adv. Funct. Mater.* **2015**, *25*, 2287−2295.

(10) Pandit, S.; Godiyal, A.; Vimal, A.; Singh, U.; Joshi, D.; Kalyanasundaram, D. An Affordable Insole-Sensor-Based Trans-Femoral Prosthesis for Normal Gait. *Sensors* **2018**, *18*, No. 706.

(11) Rus, D.; Tolley, M. T. Design, Fabrication and Control of Soft Robots. *Nature* **2015**, *521*, 467−475.

(12) Ozel, S.; Keskin, N. A.; Khea, D.; Onal, C. D. A Precise Embedded Curvature Sensor Module for Soft-Bodied Robots. *Sens. Actuators, A* **2015**, *236*, 349−356.

(13) Potyrailo, R. A. Multivariable Sensors for Ubiquitous Monitoring of Gases in the Era of Internet of Things and Industrial Internet. *Chem. Rev.* **2016**, *116*, 11877−11923.

(14) Schwartz, G.; Tee, B. C.-K.; Mei, J.; Appleton, A. L.; Kim, D. H.; Wang, H.; Bao, Z. Flexible Polymer Transistors with High Pressure Sensitivity for Application in Electronic Skin and Health Monitoring. *Nat. Commun.* **2013**, *4*, No. 1859.

(15) Lee, S.; Reuveny, A.; Reeder, J.; Lee, S.; Jin, H.; Liu, Q.; Yokota, T.; Sekitani, T.; Isoyama, T.; Abe, Y.; et al. A Transparent Bending-Insensitive Pressure Sensor. *Nat. Nanotechnol.* **2016**, *11*, 472−478.

(16) Lee, J.; Kwon, H.; Seo, J.; Shin, S.; Koo, J. H.; Pang, C.; Son, S.; Kim, J. H.; Jang, Y. H.; Kim, D. E.; Lee, T. Conductive Fiber-Based Ultrasensitive Textile Pressure Sensor for Wearable Electronics. *Adv. Mater.* **2015**, *27*, 2433−2439.

(17) Tian, H.; Shu, Y.; Wang, X.-F.; Mohammad, M. A.; Bie, Z.; Xie, Q.-Y.; Li, C.; Mi, W.-T.; Yang, Y.; Ren, T.-L. A Graphene-Based Resistive Pressure Sensor with Record-High Sensitivity in a Wide Pressure Range. *Sci. Rep.* **2015**, *5*, No. 8603.

(18) Jo, H. S.; Kwon, H.-J.; Kim, T.-G.; Park, C.-W.; An, S.; Yarin, A. L.; Yoon, S. S. Wearable Transparent Thermal Sensors and Heaters Based on Metal-Plated Fibers and Nanowires. *Nanoscale* **2018**, *10*, 19825−19834.

(19) Hong, S. Y.; Lee, Y. H.; Park, H.; Jin, S. W.; Jeong, Y. R.; Yun, J.; You, I.; Zi, G.; Ha, J. S. Stretchable Active Matrix Temperature Sensor Array of Polyaniline Nanofibers for Electronic Skin. *Adv. Mater.* **2016**, *28*, 930−935.

(20) Yang, J.; Wei, D.; Tang, L.; Song, X.; Luo, W.; Chu, J.; Gao, T.; Shi, H.; Du, C. Wearable Temperature Sensor Based on Graphene Nanowalls. *RSC Adv.* **2015**, *5*, 25609−25615.

(21) Kim, K. K.; Hong, S.; Cho, H. M.; Lee, J.; Suh, Y. D.; Ham, J.; Ko, S. H. Highly Sensitive and Stretchable Multidimensional Strain Sensor with Prestrained Anisotropic Metal Nanowire Percolation Networks. *Nano Lett.* **2015**, *15*, 5240−5247.

(22) Ryu, S.; Lee, P.; Chou, J. B.; Xu, R.; Zhao, R.; Hart, A. J.; Kim, S.-G. Extremely Elastic Wearable Carbon Nanotube Fiber Strain Sensor for Monitoring of Human Motion. *ACS Nano* **2015**, *9*, 5929−5936.

(23) Ge, J.; Sun, L.; Zhang, F. R.; Zhang, Y.; Shi, L. A.; Zhao, H. Y.; Zhu, H. W.; Jiang, H. L.; Yu, S. H. A Stretchable Electronic Fabric Artificial Skin with Pressure-, Lateral Strain-, and Flexion-Sensitive Properties. *Adv. Mater.* **2016**, *28*, 722−728.

(24) Pang, Y.; Tian, H.; Tao, L.; Li, Y.; Wang, X.; Deng, N.; Yang, Y.; Ren, T.-L. Flexible, Highly Sensitive, and Wearable Pressure and Strain Sensors with Graphene Porous Network Structure. *ACS Appl. Mater. Interfaces* **2016**, *8*, 26458−26462.

(25) Lee, T.; Choi, Y. W.; Lee, G.; Pikhitsa, P. V.; Kang, D.; Kim, S. M.; Choi, M. Transparent Ito Mechanical Crack-Based Pressure and Strain Sensor. *J. Mater. Chem. C* **2016**, *4*, 9947−9953.

(26) Zhang, F.; Zang, Y.; Huang, D.; Di, C.-a.; Zhu, D. Flexible and Self-Powered Temperature−Pressure Dual-Parameter Sensors Using Microstructure-Frame-Supported Organic Thermoelectric Materials. *Nat. Commun.* **2015**, *6*, No. 8356.

(27) An, B. W.; Heo, S.; Ji, S.; Bien, F.; Park, J.-U. Transparent and Flexible Fingerprint Sensor Array with Multiplexed Detection of Tactile Pressure and Skin Temperature. *Nat. Commun.* **2018**, *9*, No. 2458.

(28) Hsieh, H.-H.; Hsu, F.-C.; Chen, Y.-F. Energetically Autonomous, Wearable, and Multifunctional Sensor. *ACS Sens.* **2018**, *3*, 113−120.

DOI: 10.1021/acsami.9b12847
ACS Appl. Mater. Interfaces 2019, 11, 40232−40242

(29) Luo, C.; Jia, J.; Gong, Y.; Wang, Z.; Fu, Q.; Pan, C. Highly Sensitive, Durable, and Multifunctional Sensor Inspired by a Spider. *ACS Appl. Mater. Interfaces* **2017**, *9*, 19955−19962.
(30) Hua, Q.; Sun, J.; Liu, H.; Bao, R.; Yu, R.; Zhai, J.; Pan, C.; Wang, Z. L. Skin-Inspired Highly Stretchable and Conformable Matrix Networks for Multifunctional Sensing. *Nat. Commun.* **2018**, *9*, No. 244.
(31) Xu, H.; Lu, Y. F.; Xiang, J. X.; Zhang, M. K.; Zhao, Y. J.; Xie, Z. Y.; Gu, Z. Z. A Multifunctional Wearable Sensor Based on a Graphene/Inverse Opal Cellulose Film for Simultaneous, in Situ Monitoring of Human Motion and Sweat. *Nanoscale* **2018**, *10*, 2090−2098.
(32) Kim, D.-Y.; Sinha-Ray, S.; Park, J.-J.; Lee, J.-G.; Cha, Y.-H.; Bae, S.-H.; Ahn, J.-H.; Jung, Y. C.; Kim, S. M.; Yarin, A. L.; Yoon, S. S. Self-Healing Reduced Graphene Oxide Films by Supersonic Kinetic Spraying. *Adv. Funct. Mater.* **2014**, *24*, 4986−4995.
(33) Lee, J. G.; Kim, D. Y.; Lee, J. H.; Sinha-Ray, S.; Yarin, A. L.; Swihart, M. T.; Kim, D.; Yoon, S. S. Production of Flexible Transparent Conducting Films of Self-Fused Nanowires Via One-Step Supersonic Spraying. *Adv. Funct. Mater.* **2017**, *27*, No. 1602548.
(34) Kim, T.-G.; Lee, J.-G.; Park, C.-W.; Jo, H.-S.; Kim, M.-W.; van Hest, M. F.; Cho, D.-H.; Chung, Y.-D.; Yoon, S. S. Effect of Supersonic Spraying Impact Velocity on Opto-Electric Properties of Transparent Conducting Flexible Films Consisting of Silver Nanowire, Ito, and Polyimide Multilayers. *J. Alloys Compd.* **2018**, *739*, 653−659.
(35) Lee, J.-G.; Lee, J.-H.; An, S.; Kim, D.-Y.; Kim, T.-G.; Al-Deyab, S. S.; Yarin, A. L.; Yoon, S. S. Highly Flexible, Stretchable, Wearable, Patternable and Transparent Heaters on Complex 3d Surfaces Formed from Supersonically Sprayed Silver Nanowires. *J. Mater. Chem. A* **2017**, *5*, 6677−6685.
(36) Enser, H.; Kulha, P.; Sell, J. K.; Schatzl-Linder, M.; Strauß, B.; Hilber, W.; Jakoby, B. Printed Strain Gauges Embedded in Organic Coatings-Analysis of Gauge Factor and Temperature Dependence. *Sens. Actuators, A* **2018**, *276*, 137−143.
(37) Wagner, S.; Yim, C.; McEvoy, N.; Kataria, S.; Yokaribas, V.; Kuc, A.; Pindl, S.; Fritzen, C.-P.; Heine, T.; Duesberg, G. S. Highly Sensitive Electromechanical Piezoresistive Pressure Sensors Based on Large-Area Layered Ptse2 Films. *Nano Lett.* **2018**, *18*, 3738−3745.
(38) Chun, S.; Choi, Y.; Park, W. All-Graphene Strain Sensor on Soft Substrate. *Carbon* **2017**, *116*, 753−759.
(39) Sheng, H.; Zhang, X.; Ma, Y.; Wang, P.; Zhou, J.; Su, Q.; Lan, W.; Xie, E.; Zhang, C. J. Ultrathin, Wrinkled, Vertically Aligned Co (Oh) 2 Nanosheets/Ag Nanowires Hybrid Network for Flexible Transparent Supercapacitor with High Performance. *ACS Appl. Mater. Interfaces* **2019**, *11*, 8992−9001.
(40) Lan, W.; Chen, Y.; Yang, Z.; Han, W.; Zhou, J.; Zhang, Y.; Wang, J.; Tang, G.; Wei, Y.; Dou, W.; et al. Ultraflexible Transparent Film Heater Made of Ag Nanowire/PVA Composite for Rapid-Response Thermotherapy Pads. *ACS Appl. Mater. Interfaces* **2017**, *9*, 6644−6651.
(41) Nateghi, M. R.; Shateri-Khalilabad, M. Silver Nanowire-Functionalized Cotton Fabric. *Carbohydr. Polym.* **2015**, *117*, 160−168.
(42) Ravanat, J.-L.; Douki, T.; Cadet, J. Direct and Indirect Effects of UV Radiation on DNA and Its Components. *J. Photochem. Photobiol., B* **2001**, *63*, 88−102.
(43) Sinha, R. P.; Häder, D.-P. UV-Induced DNA Damage and Repair: A Review. *Photochem. Photobiol. Sci.* **2002**, *1*, 225−236.
(44) Brenner, M.; Hearing, V. J. The Protective Role of Melanin against UV Damage in Human Skin. *Photochem. Photobiol.* **2008**, *84*, 539−549.
(45) Jo, H. S.; An, S.; Lee, J.-G.; Park, H. G.; Al-Deyab, S. S.; Yarin, A. L.; Yoon, S. S. Highly Flexible, Stretchable, Patternable, Transparent Copper Fiber Heater on a Complex 3d Surface. *NPG Asia Mater.* **2017**, *9*, No. e347.
(46) Sadasivuni, K. K.; Kafy, A.; Zhai, L.; Ko, H. U.; Mun, S.; Kim, J. Transparent and Flexible Cellulose Nanocrystal/Reduced Graphene Oxide Film for Proximity Sensing. *Small* **2015**, *11*, 994−1002.
(47) Wei, Y.; Torah, R.; Li, Y.; Tudor, J. Dispenser Printed Capacitive Proximity Sensor on Fabric for Applications in the Creative Industries. *Sens. Actuators, A* **2016**, *247*, 239−246.
(48) Kulkarni, M. R.; John, R. A.; Rajput, M.; Tiwari, N.; Yantara, N.; Nguyen, A. C.; Mathews, N. Transparent Flexible Multifunctional Nanostructured Architectures for Non-Optical Readout, Proximity, and Pressure Sensing. *ACS Appl. Mater. Interfaces* **2017**, *9*, 15015−15021.
(49) Ma, R.; Tsukruk, V. V. Seriography-Guided Reduction of Graphene Oxide Biopapers for Wearable Sensory Electronics. *Adv. Funct. Mater.* **2017**, *27*, No. 1604802.
(50) Halliday, D.; Walker, J.; Resnick, R. *Fundamentals of Physics*; John Wiley & Sons: New York City, 2013.
(51) Kogut, L.; Komvopoulos, K. Electrical Contact Resistance Theory for Conductive Rough Surfaces. *J. Appl. Phys.* **2003**, *94*, 3153−3162.
(52) Holm, R. *Electric Contacts: Theory and Application*; Springer-Verlag: Berlin/Heidelberg, Germany, 2013.
(53) Timsit, R. S. Electrical Contact Resistance: Properties of Stationary Interfaces. *IEEE Trans. Compon. Packag. Technol.* **1999**, *22*, 85−98.
(54) Landau, L. D.; Lifshitz, E. M. *Theory of Elasticity*; Pergamon Press: Oxford, U.K., 1970; Vol. 7.
(55) Shi, G.; Zhao, Z.; Pai, J. H.; Lee, I.; Zhang, L.; Stevenson, C.; Ishara, K.; Zhang, R.; Zhu, H.; Ma, J. Highly Sensitive, Wearable, Durable Strain Sensors and Stretchable Conductors Using Graphene/Silicon Rubber Composites. *Adv. Funct. Mater.* **2016**, *26*, 7614−7625.
(56) Amjadi, M.; Kyung, K. U.; Park, I.; Sitti, M. Stretchable, Skin-Mountable, and Wearable Strain Sensors and Their Potential Applications: A Review. *Adv. Funct. Mater.* **2016**, *26*, 1678−1698.
(57) Shi, G.; Araby, S.; Gibson, C. T.; Meng, Q.; Zhu, S.; Ma, J. Graphene Platelets and Their Polymer Composites: Fabrication, Structure, Properties, and Applications. *Adv. Funct. Mater.* **2018**, *28*, No. 1706705.
(58) Kuczynski, G. Effect of Elastic Strain on the Electrical Resistance of Metals. *Phys. Rev.* **1954**, *94*, 61.
(59) Parker, R.; Krinsky, A. Electrical Resistance-Strain Characteristics of Thin Evaporated Metal Films. *J. Appl. Phys.* **1963**, *34*, 2700−2708.
(60) Angelidis, N.; Wei, C.; Irving, P. The Electrical Resistance Response of Continuous Carbon Fibre Composite Laminates to Mechanical Strain. *Composites, Part A* **2004**, *35*, 1135−1147.
(61) Pelot, D.; Jun, S.; Yarin, A. Bentonite Dispersions: Transition from Liquid-Like to Solid-Like Behavior and Cracking. *J. Non-Newtonian Fluid Mech.* **2015**, *219*, 50−64.
(62) Choi, M. K.; Park, O. K.; Choi, C.; Qiao, S.; Ghaffari, R.; Kim, J.; Lee, D. J.; Kim, M.; Hyun, W.; Kim, S. J.; et al. Cephalopod-Inspired Miniaturized Suction Cups for Smart Medical Skin. *Adv. Healthcare Mater.* **2016**, *5*, 80−87.
(63) Gu, Z.; Wan, X.; Lou, Z.; Zhang, F.; Shi, L.; Li, S.; Dai, B.; Shen, G.; Wang, S. Skin Adhesives with Controlled Adhesion by Polymer Chain Mobility. *ACS Appl. Mater. Interfaces* **2019**, *11*, 1496−1502.

DOI: 10.1021/acsami.9b12847
ACS Appl. Mater. Interfaces 2019, 11, 40232−40242